Journal of
Water & Climate Change

IWA PUBLISHING

Journal of Water and Climate Change Vol 14 No 7, 2448 doi: 10.2166/wcc.2023.136

Identification and evolution characteristics of drought field in the Pearl River Basin based on REOF-ESMD

Minhua Ling[a], Xiaoyue Hu[a], Xiaomin Guo[a] and Lili Yu[b,*]

[a] School of Water Conservancy Engineering, Zhengzhou University, Zhengzhou 450001, China
[b] General Institute of Water Resources and Hydropower Planning and Design, Ministry of Water Resources, Beijing 100032, China
*Corresponding author. E-mail: yull666888@163.com

ABSTRACT

The traditional drought field studies are inadequate to study drought field characteristics from the perspective of trend and periodicity at the same time, especially to compare the interannual and interdecadal variations of different drought types in the drought field to reveal their similarity and difference patterns. The drought field in Pearl River Basin (PRB) was determined in this paper using the standardized precipitation evapotranspiration index (SPEI) and the empirical orthogonal function (EOF)/rotated empirical orthogonal function (REOF). Periodic characteristics and trend features of the drought field were recognized by extreme-point symmetric mode decomposition (ESMD) and other methods. The results showed that from the perspective of regional characteristics five different spatial modes may be used to categorize the interannual drought field of the PRB; there were interannual cycles associated with the southwest-type drought and the northwest-type drought. The central-south-, north-central- and eastern-type droughts had both interannual and interdecadal cycles; during the study period, the PRB's five types of drought revealed a changing tendency as opposed to a straightforward linear trend; from the interannual variation, the southwest-type drought was consistent with the northwest-type drought prior to 2000, and the north-central-type drought was consistent with the eastern-type drought before 2010.

Key words: drought field, EOF/REOF, ESMD, interannual variation, interdecadal variation, Pearl River Basin

HIGHLIGHTS

- The spatial characteristics and periodic properties of the watershed were identified.
- There are five spatial modes in the Pearl River Basin.
- Southwestern and northwestern droughts have interannual cycles.
- Five types of droughts in the Pearl River Basin showed a fluctuating trend.
- The interannual similarity and variability of the five droughts were studied.

GRAPHICAL ABSTRACT

How do you describe the type of drought in the Pearl River Basin **drought field**?
What methods can be used to clearly study the **trend features and cycle characteristics** of different drought types?
What are the similarities and differences in the characteristics of **interannual variability and** interdecadal **variability** of different drought types?

Method:
standardized precipitation evapotranspiration index (SPEI)
empirical orthogonal function (EOF)
rotated empirical orthogonal function (REOF)
extreme-point symmetric mode decomposition (ESMD)
fast Fourier transform (FFT)
pearson correlation analysis

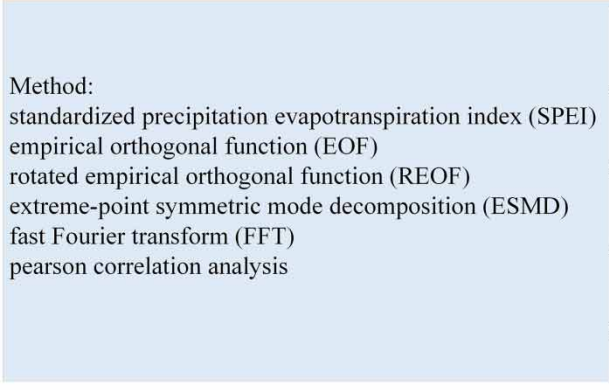

Five drought types in the distribution of drought field in the Pearl River Basin

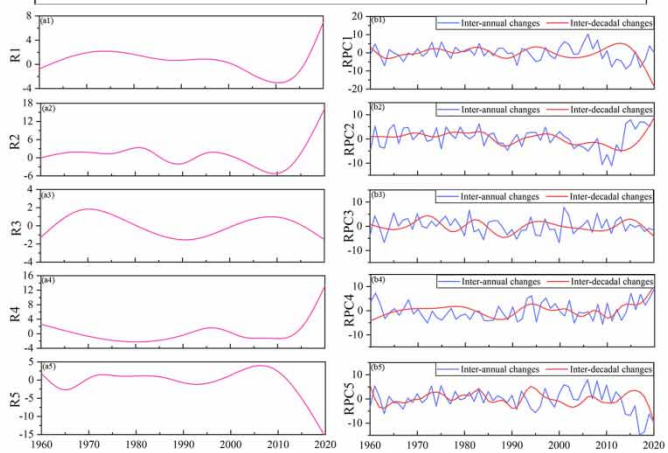

Left: trend variation characteristics of drought types
Right: interannual and interdecadal comparison curves of drought types

1. INTRODUCTION

When there is a lack of water due to prolonged low humidity levels, it is referred to as a drought (Band *et al.* 2022). This phenomenon has an adverse effect on a variety of natural systems, as well as some industries and economic sectors (Van Loon *et al.* 2016; Won *et al.* 2020). The climate has been undergoing extensive and rapid changes during the past century, and human activities have caused the atmosphere, oceans and land to warm, according to the Sixth Assessment Report of the UN Intergovernmental Panel on Climate Change (Sun 2021). Drought is occurring at an increasing frequency, causing unpredictable losses around the world (Heudorfer & Stahl 2017; Sahana *et al.* 2021; Ling *et al.* 2022; Zhan *et al.* 2022). Therefore, it is important to study the characteristics of drought changes in order to explore the mechanism of drought causes and guide the government in disaster prevention and mitigation.

The climate variable field of a particular region or watershed usually consists of many observation stations or grid points, which are time-varying and quite complex in practice (Gbetibouo & Hassan 2005). How to find its main spatial distribution characteristics and its time variation law is the focus of the study. If a few spatial modes with a small number can be used to describe the original variable field and can basically not cover the information of the original variable field, the spatial and

temporal variation characteristics of the original variable field can be better obtained (Ureta *et al.* 2020). The quantification of climate element fields based on empirical orthogonal function (EOF) and rotated empirical orthogonal function (REOF) has been widely carried out in recent years to achieve the spatial and temporal decomposition of climate fields at regional or watershed scale (Bi *et al.* 2021; Saharwardi & Kumar 2022). The EOF/REOF allows the decomposition of the climate field into a spatial mode, which describes the variability structure of the climate variable field over the entire region, and a time mode, which reflects the weight changes of the corresponding spatial modes over time (Zhou *et al.* 2020). The drought field, like the precipitation field, is a climatic element field, which can clearly reflect the spatial distribution characteristics of drought in a certain region or watershed (Jeong *et al.* 2010). Compared with the EOF method, the REOF method focuses on local characteristics, and the drought field obtained by decomposition is clearer in space, which can identify the spatial distribution characteristics of regional or watershed drought more accurately, and the results achieved have been more fruitful. For example, Zhao *et al.* (2019) analyzed the spatial characteristics of drought and flood disasters by using EOF and REOF methods based on the historical drought and flood level series of 36 stations in the middle and lower reaches of the Yellow River from 1470 to 1911 reconstructed through historical literature. Based on the drought index and 70 monthly circulation indices in northwest China, Qi *et al.* (2020) analyzed the interannual and interdecadal characteristics of drought and the spatial and temporal responses to different circulation indices in northwest China in the past 36 years by using REOF and random forest methods.

Extreme-point symmetric mode decomposition (ESMD) is not only adaptive to data but also has unique advantages in trend separation and period analysis of time series (Wang & Li 2013; Feng & Su 2019). This method effectively solves the problem of 'modal confusion' of empirical mode decomposition (EMD), overcomes the interference of adding white noise to the original signal decomposition in ensemble empirical mode decomposition (EEMD) and avoids the artificial subjectivity of choosing the basis function of wavelet transform (Zhou *et al.* 2019; Xie *et al.* 2022).

Meteorological drought is the root cause of agricultural drought, hydrological drought and socioeconomic drought. There are many meteorological drought indices, commonly used as standardized precipitation index (SPI), Palmer drought severity index (PDSI) and standardized precipitation evapotranspiration index (SPEI). SPEI combines the advantages of both SPI and PDSI, which not only considers multifactor variables but also has multiple timescales, and thus is widely used for spatial and temporal analysis of drought (Jiang *et al.* 2017; Shi *et al.* 2020; Zhang *et al.* 2021).

In this paper, we construct the REOF-ESMD model, that is, by calculating the annual-scale SPEI, using the EOF/REOF method to decompose the regional or watershed drought field in time and space and then quantify the time coefficients corresponding to different spatial modes by ESMD in order to achieve the purpose of spatio-temporal coupling analysis.

Water resources are essential in the Pearl River Basin (PRB) because of its high socioeconomic development. Despite the PRB being dominated by a subtropical monsoon climate and being located in humid regions with abundant precipitation, increasingly frequent and severe droughts have recently been caused by profound climatic changes and associated human activities (Barriopedro *et al.* 2012; Sun *et al.* 2022). As a result, understanding and assessing the evolution of the drought in the PRB is crucial for monitoring, evaluating and predicting it. Severe droughts occurred in the PRB in 1963, 1998–1999, 2003–2004, 2007 and 2009–2010 (Huang *et al.* 2019). In this regard, several scholars have carried out studies on the risk of drought (Huang *et al.* 2013), the monitoring of drought (Deng *et al.* 2020) and the causes of drought (Luo *et al.* 2017) in the PRB. From these studies, the study of the drought field in the PRB needs to be strengthened. For example, Jing *et al.* (2021) only used the EOF method to identify the drought field in the PRB from 1960 to 2019 and did not use REOF method to identify the spatial distribution characteristics of drought in the watershed more precisely. Based on the multi-timescale SPEI of the PRB from 1961 to 2011, Chen (2020) applied REOF and wavelet analysis methods to analyze the spatial distributions and temporal variation characteristics of drought in the watershed during this period. On the one hand, the study period is only up to 2011, but droughts in the PRB have increased in frequency in latest years, especially from October 2020 to September 2021, the precipitation in the PRB was 60–70% less, which was the lowest in the same period since 1961, resulting in severe drought (Qian & Lu 2022). Thus, it is necessary to study the drought in the PRB at a longer timescale, which can help to better reveal its spatial and temporal characteristics of drought. On the other hand, the analysis method of wavelet analysis is subjective in the selection of basis functions, which will affect the results to some extent (Song & Chen 2021), and the study lacks interannual and interdecadal comparisons among subregions.

Therefore, this paper calculates the annual timescale SPEI based on the measured monthly meteorological data from 1960 to 2020 in the PRB, applies the EOF/REOF method to identify the drought field in the PRB and uses the ESMD method to analyze the temporal evolution characteristics (cycle and trend characteristics) and to explore the similarity and difference

patterns of interannual and interdecadal changes of different types. This method enriches the study of drought field and can offer a scientific basis for drought monitoring and forecasting.

2. DATA AND METHODS

2.1. Research area

Along China's southern coast, the PRB is situated in the tropical and subtropical monsoon climate zone, with the Nanling Mountains in the north, the South China Sea in the south and the Yunnan-Guizhou Plateau in the west. The PRB is located between 102°14′–115°57′ E and 21°35′–26°50′ N, with a large east–west span. The PRB spans over 442,100 km^2 in total, involving the six provinces of Yunnan, Guizhou, Guangxi, Guangdong, Hunan and Jiangxi. The basin is blessed with abundant water, sunshine and accumulated temperature and is an important rice-, sugar-producing area and subtropical and tropical crop cultivation area. The distribution of the precipitation is unequal both in terms of time and space, despite the fact that it is abundant on average each year (1,200–2,200 mm). In time, the rainy period is mainly from April to September every year, while the rainless period is mainly from December to February of the following year. Spatially, the precipitation in the northeast is greater than that in the southwest. The average temperature for many years is 14–22 °C, and the temperature is relatively mild. According to *The Third National Water Resources Survey and Assessment*, the PRB is divided into 14 three-level water resource zones, with 100 national meteorological stations (Table 1 and Figure 1).

2.2. Data sources

The Geospatial Data Cloud (http://www.gscloud.cn/) provided the essential spatial data for the PRB, including the 90 m × 90 m digital elevation model and the national boundary vector data downloaded by Chinese Academy of Environmental Sciences. The China Meteorological Data Network (http://data.cma.cn/) was used to collect monthly weather information from 100 meteorological stations in the PRB between 1960 and 2020, which were precipitation (p), relative humidity (RH), temperature (T), sunshine hours (n) and atmospheric pressure (P). The stations with three or more months of missing data were discarded, and the very few missing data were interpolated using linear regression of adjacent stations to ensure their continuity.

2.3. Methods

2.3.1. Standardized precipitation evapotranspiration index

The SPEI which considers multifactor variables can usually be calculated by the Thornthwaite model and Penman–Monteith model. The former only considers temperature, while the latter includes solar radiation, wind speed and spatial location of the

Table 1 | Third-level water resource zones in the PRB

Brief title	Full name
BPJ	Beipanjiang River
NPJ	Nanpanjiang River
LJ	Liujiang River
HSH	Hongshui River
YJ	Youjiang River
GHJ	Guihe River
ZJ	Zuo and Yujiang Rivers
QXJ	Qianxun and Xijiang Rivers
BJ1	Beijiang River upstream of Dakengkou City
BJ2	Beijiang River downstream of Dakengkou City
XB	Delta of Xijiang and Beijiang Rivers
DJ1	Dongjiang River upstream of Qiuxiang River Estuary
DJ2	Dongjiang River downstream of Qiuxiang River Estuary
DJS	Dongjiang River Delta

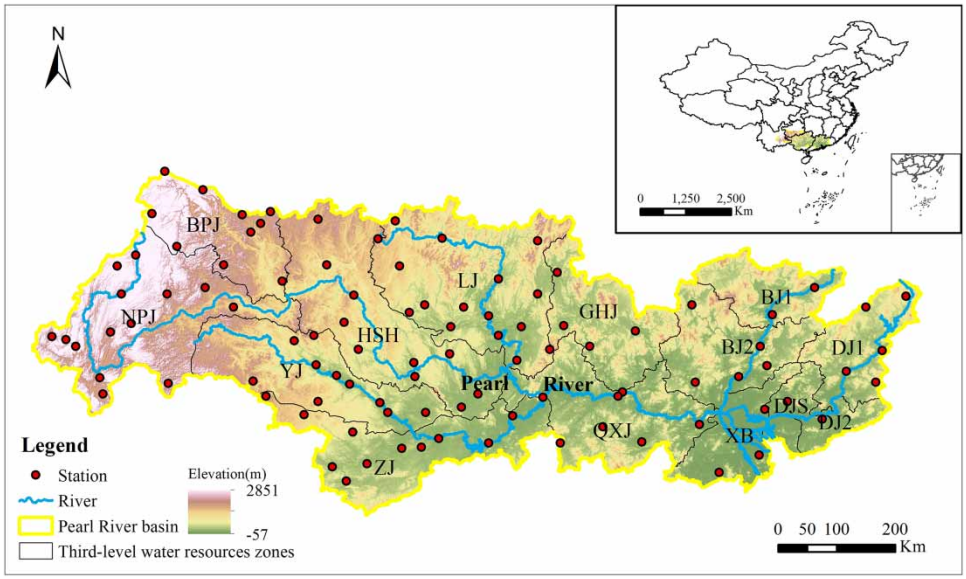

Figure 1 | Geographical location of tertiary zones and meteorological stations in the PRB.

station in addition to temperature (Chen & Sun 2015). In this study, the Penman–Monteith model (Zuo *et al.* 2019) was used to calculate the SPEI. SPEI-12 represents the annual SPEI values.

2.3.2. Empirical orthogonal function/rotated empirical orthogonal function

2.3.2.1. Empirical orthogonal function. EOF was first proposed by Pearson. Lorenz introduced it to the field of atmospheric science in the 1950s, and then the method was widely used (Kim *et al.* 2015).

The main elements of the EOF analysis method are as follows:

The observations of a climate variable field are given in matrix form:

$$X_{m\times n}=\begin{pmatrix} x_{11} & x_{12} & \cdots & x_{1n} \\ x_{21} & x_{22} & \cdots & x_{2n} \\ & \cdots & \cdots & \\ x_{m1} & x_{m2} & \cdots & x_{mn} \end{pmatrix}$$

m denotes the number of meteorological stations and n denotes the length of the series.

A natural orthogonal expansion is performed on the meteorological time series:

$$X_{m\times n}=\mathrm{EOF}_{m\times m}\times \mathrm{PC}_{m\times n}$$

Each column of the $\mathrm{EOF}_{m\times m}$ matrix is an eigenvector, which is also called a spatial mode. Generally, the distribution of the eigenvector corresponding to each eigenvalue in space is called a mode. Each row of the $\mathrm{PC}_{m\times n}$ matrix is the time coefficient of the eigenvector.

The variance contribution of each spatial mode is also calculated in the EOF analysis to measure the weight of their contribution to the original matrix. The contribution of the kth eigenvector to the matrix A is

$$\rho_k=\frac{\lambda_k}{\sum_{i=1}^{m}\lambda_i}(k=1,2,\ \ldots,p;p<m)$$

The cumulative variance contribution of the first p eigenvectors (spatial modalities) is

$$G = \frac{\sum_{i=1}^{p} \lambda_i}{\sum_{j=1}^{m} \lambda_j} (p < m)$$

After the EOF analysis, the obtained spatial modes are also tested for significance. In this paper, the significance test is performed using the error range of eigenvalue calculation proposed by North *et al.* (1982), and the error range of eigenvalues is

$$e_i = \lambda_i \left(\frac{2}{m}\right)^{\frac{1}{2}}$$

The error ranges are labeled sequentially, and if there is an overlap between the two preceding and following error ranges, they do not pass the significance test (Li *et al.* 2019).

2.3.2.2. Rotated empirical orthogonal function. The REOF method is also a typological zoning method for climate, which can reflect not only the variability of different regions but also the relevant distribution of each region.

EOF serves as the foundation for REOF. REOF intercepts several eigenvectors whose cumulative variance reaches a certain standard and then carries out the maximum orthogonal rotation of variance. Finally, the high load vectors are commonly concentrated in a few variables, while the load values of other regions are proximity to zero so that the information features of the original element field are centrally mapped to the dominant spatial pattern represented by the load field. If the EOF intercepts, the first k eigenvectors and the cumulative variance contribution reaches a certain value, these k eigenvectors can be adjusted again by the REOF maximum orthogonal rotation transformation, so that the cumulative variance contribution of the adjusted k eigenvectors still maintains the value, but the individual eigenvectors reflect the local information of the field as much as possible. Corresponding to the EOF decomposition, each column of the $\mathrm{REOF}_{m\times m}$ matrix is an eigenvector, also known as a spatial mode, and each row of the $\mathrm{RPC}_{m\times n}$ matrix corresponds to the time coefficient of the eigenvector (Hang *et al.* 2022).

MATLAB was used for both EOF and REOF calculations.

2.3.3. Extreme-point symmetric mode decomposition

ESMD was developed from EMD. ESMD uses internal extreme-point symmetric interpolation instead of outer envelope interpolation. The optimization strategy is adopted to ensure that the trend function and selection times are optimal, which solves the mode aliasing problem caused by frequency crossover in the application of EMD. To achieve the transformation from local self-adaptation to global self-adaptation, the final vestigial mode is optimized using the least square method. The most optimal selection times can yield two portions: a series of intrinsic mode function (IMF) components and a trend item R. When the variance ratio of the trend item R is minimal, the ESMD reaches the optimal state and stops automatically (Wang *et al.* 2022). The ESMD calculations were performed using the toolkit provided by Wang & Li (2013).

The specific process of this decomposition method is as follows:

(1) Suppose a time series is x, find all the maximum points and minimum points, denoted as A $(1 \le i \le n)$.
(2) Connect all adjacent A with line segments, noting their midpoints as M $(1 \le i \le n-1)$, and add the boundary midpoints to the left and right ends.
(3) Construct q interpolation curves $C_1, C_2, \ldots, C_q\,(q \ge 1)$ using $n+1$ midpoints and calculate their average value $C = (C_1 + C_2 + \cdots + C_q)/q$.
(4) Repeat the above three steps for the sequence $x - C$ until $C \le \varepsilon$ or the number of screenings reaches a pregiven maximum value K to obtain the first IMF component IMF1.
(5) Repeat the above four steps for the remaining sequence x-IMF1 until the remaining sequence R is no longer greater than a pregiven extreme value point to obtain the IMF components IMF2, IMF3, ….

(6) Change the value of K in the limited interval $[K_{\min}, K_{\max}]$ and repeat the above five steps to find the variance of the sequence x-R_0 and plot the K and σ/σ_0 to find the K_0 corresponding to the minimum value of σ/σ_0 in the plot. Repeating the above five steps again with K_0 as the constraint, we finally obtain the adaptive global mean R of the series, which is the trend item of the series.

Finally, the original time series can be expressed as $x = \sum_{i=1}^{n} IMF_i + R$, i.e., the time series is decomposed into a series of IMF components and a trend item R using the ESMD method.

2.3.4. Pearson correlation analysis

This study explores the closeness of the IMF components, the trend item R and the original time series by examining the correlation between them. The linear relationship between the two variables is evaluated using the Pearson correlation coefficient. Suppose there are t sets of data, for (a_i, b_i) $(i = 1, 2, \ldots, t)$, this is the specific calculating formula:

$$r = \frac{\sum_{i=1}^{t} (a_i - \bar{a})(b_i - \bar{b})}{\sqrt{\sum_{i=1}^{t} (a_i - \bar{a})^2 \sum_{i=1}^{t} (b_i - \bar{b})^2}}$$

where r is a real number between $[-1,1]$. When r is between $[-1,0)$, there is a negative correlation between variables, and when r is between $(0,1]$, there is a positive correlation between variables. When the value of $|r|$ is large, the correlation is strong, while when the value of $|r|$ is small, the correlation is weak. To prevent false correlation, a significance test is needed. The probability α is called the significance level, and α is usually taken as 0.01 or 0.05. When the significant coefficient $P < 0.01$ and $P < 0.05$, it means that it passes the significance test of $\alpha = 0.01$ (passing the 1% significance level test) and $\alpha = 0.05$ (passing the 5% significance level test), respectively (Song *et al.* 2018).

2.3.5. Fast Fourier transform

Discrete Fourier transform (DFT) is the most basic way of digital signal processing, which can transform the time domain signal to frequency domain and analyze the signal in frequency domain. Fast Fourier transform (FFT) is a fast algorithm for DFT, which can transform the signal from time domain to frequency domain faster. It is a big improvement compared with the lack of real-time performance due to the large amount of DFT computation (Duhamel & Vetterli 1990). MATLAB was used for the calculation of FFT.

Assume a data time domain sequence as follows:

$$x(n) = \begin{cases} x(nT_1), & 0 \leqslant n \leqslant N_0 - 1 \\ 0, & N_0 \leqslant n \leqslant N \end{cases}$$

Then its frequency domain transformation is as follows:

$$X(k) = \sum_{n=0}^{N-1} x(nT_1) \mathrm{e}^{-j\left(\frac{2\pi}{N}\right)nk}, \quad 0 \leqslant n \leqslant N - 1$$

Spectrum $X(k)$ consists of real part $U(k)$ and imaginary part $U(k)$:

$$X(k) = U(k) + V(k)$$

Then the amplitude spectrum $A(k)$ and the phase spectrum $\varphi(k)$ in the frequency spectrum are as follows:

$$A(k) = |X(k)|, \quad \varphi(k) = \arctan\frac{V(k)}{U(k)}$$

2.3.6. The research route

(1) The annual SPEI values (SPEI-12) were calculated from the monthly meteorological data measured from 1960 to 2020 in the PRB.
(2) The EOF was used to decompose the spatial modes depending on the SPEI-12 to identify overall drought characteristics in the PRB.
(3) To get spatial modes and temporal coefficients, REOF decomposition was performed based on EOF decomposition, and the local characteristics of the drought field were identified by spatial modes. Points (2) and (3) are collectively called 'drought field identification'.
(4) ESMD was used to decompose the time coefficients (RPC) of REOF to obtain the IMF components and trend item *R*. The correlation strength between the IMF components, trend item *R* and the original time coefficient series was measured using the Pearson correlation coefficient.
(5) FFT was performed on the IMF components to identify the periodic characteristics of the drought field, and the trend features of trend item *R* were evaluated to disclose the evolution features of the drought field.

Figure 2 displays the study's research roadmap.

3. RESULTS AND DISCUSSION

3.1. Identification of drought field

SPEI-12 from 1960 to 2020 was decomposed using EOF. Only the first five modes did not overlap and passed the North et al.'s significance test, whose cumulative variance contribution rate reached 63.94% (Table 2). The convergence speed of the total variance contribution rate of the mode was slow due to the large climate difference between different regions in the PRB. Except for the first few modes, the variance contribution rate of the latter modes was small, so only the first five modes that passed the North et al.'s significance test were orthogonally rotated with maximum variance to obtain five modes (Table 2). Table 2 displays that the cumulative variance contribution rate of the first five modes was still 63.94% after REOF decomposition, and the variance contribution rate was redistributed among the modes.

3.1.1. Spatial characteristics of the SPEI-12 by EOF decomposition

Table 2 shows that the cumulative variance contribution rate of the first three modes obtained by EOF decomposition was in excess of 50%, and the variance contribution rate of the latter modes was relatively small, so only the first three modes were

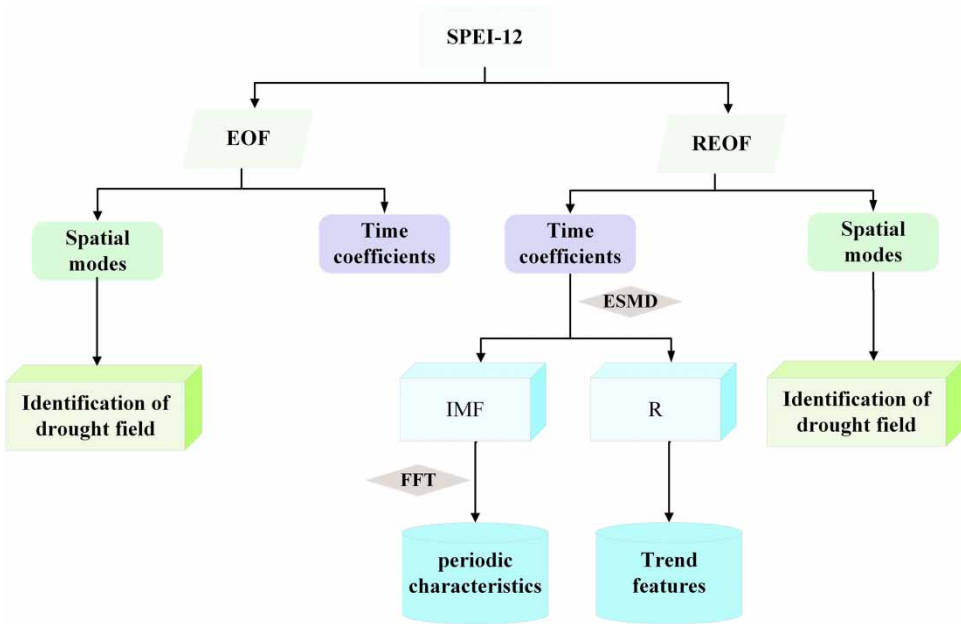

Figure 2 | Research roadmap.

Table 2 | Variance contribution and cumulative variance contribution of the first five modes

	EOF		REOF	
Mode	Variance contribution (%)	Cumulative variance contribution (%)	Variance contribution (%)	Cumulative variance contribution (%)
1	34.86	34.86	13.42	13.42
2	12.46	47.32	13.02	26.44
3	7.67	54.98	12.68	39.12
4	5.67	60.65	12.59	51.71
5	3.29	63.94	12.24	63.94

mainly analyzed. The variance contribution rate of mode 1 was 34.86%, which was much higher than that of the other modes, and it was the main spatial distribution type of the meteorological drought field in the PRB. The variance contribution rates of mode 2 and mode 3 were 12.46 and 7.67%, respectively, which were the typical spatial distribution types of meteorological drought field in the PRB. Using ArcGIS software, the spatial distributions of mode 1, mode 2 and mode 3 were obtained by the inverse distance weighting method (Figure 3).

Figure 3(a) shows that the eigenvectors of mode 1 were all positive, indicating that the trend of dry and wet changes in the PRB over 61 years was consistent; that is, the whole basin was dry or wet. The areas with high values were primarily found south of Liujiang River, southeast of Hongshui River, west of Guihe River and in a few areas of the Youjiang River, which were sensitive to the alternation of dry and wet changes. The low-value areas were found north of the Beipanjiang River, Hongshui River and certain Beijiang River regions downstream of Dakengkou City. Overall, the PRB's high value areas were concentrated in its center, with the outlying areas' values generally on the decline.

Figure 3(b) shows that the high value areas of the eigenvector in mode 2 were concentrated in the west of the PRB, while the PRB's east side was where the low-value lands were located, showing a decreasing trend from west to east, with positive values in the west and negative values in the east. The dry and wet conditions in the east and west were opposite, that is, the west was wet and the east was dry or the west was dry and the east was wet.

Figure 3(c) shows that the high value areas of the eigenvector in mode 3 were mostly located in the southwestern part of the Nanpanjiang River, and the Zuo and Yujiang Rivers, while the low-value areas were mostly found in the northwestern part of the Guihe River, the north of the Liujiang River and the northern part of the Hongshui River, showing the reverse distribution characteristics of positive in the west and south and negative in the north, that is, wet in the west and south, dry in the north or dry in the west and south, wet in the north.

Therefore, from the spatial variability of the whole region, we could divide the interannual drought field in the PRB into three types, namely the whole basin consistent type, the east–west antiphase type and the west, south–north antiphase type.

3.1.2. Spatial characteristics of the SPEI-12 by REOF decomposition

Table 2 demonstrates that the variance contribution rate of the first five modes derived by REOF decomposition did not significantly differ from one another. Therefore, the first five modes were analyzed. The spatial distributions of the first five modes of REOF were obtained by the inverse distance weighting method using ArcGIS software (Figure 4).

The high value areas of mode 1 were mostly concentrated in the Youjiang River, Zuo and Yujiang Rivers in the southwestern part of the PRB, and the maximum values were concentrated in the northwestern part of the Zuo and Yujiang Rivers. The high value areas of mode 2 were mostly concentrated in the Beipanjiang River and Nanpanjiang River in the northwest part of the PRB, and the maximum values were concentrated in the west-central of the Beipanjiang River. The high value areas of mode 3 were mostly concentrated in the Zuo and Yujiang Rivers and Qianxun and Xijiang Rivers in the south-central part of the PRB, and the maximum values were concentrated in the eastern part of the Zuo and Yujiang Rivers. The high value areas of mode 4 were mostly concentrated in the Liujiang River in the north-central part of the PRB, and the maximum values were concentrated in the eastern part of the Liujiang River. The high value areas of mode 5 were mostly concentrated in the Dongjiang River upstream/downstream of Qiuxiang River Estuary in the eastern part of the PRB, and the maximum values were mainly concentrated in the eastern part of them.

In summary, from the perspective of regional characteristics, we could divide the interannual drought field in the PRB into five types, namely the southwest-type drought corresponding to mode 1, the northwest-type drought corresponding to mode 2,

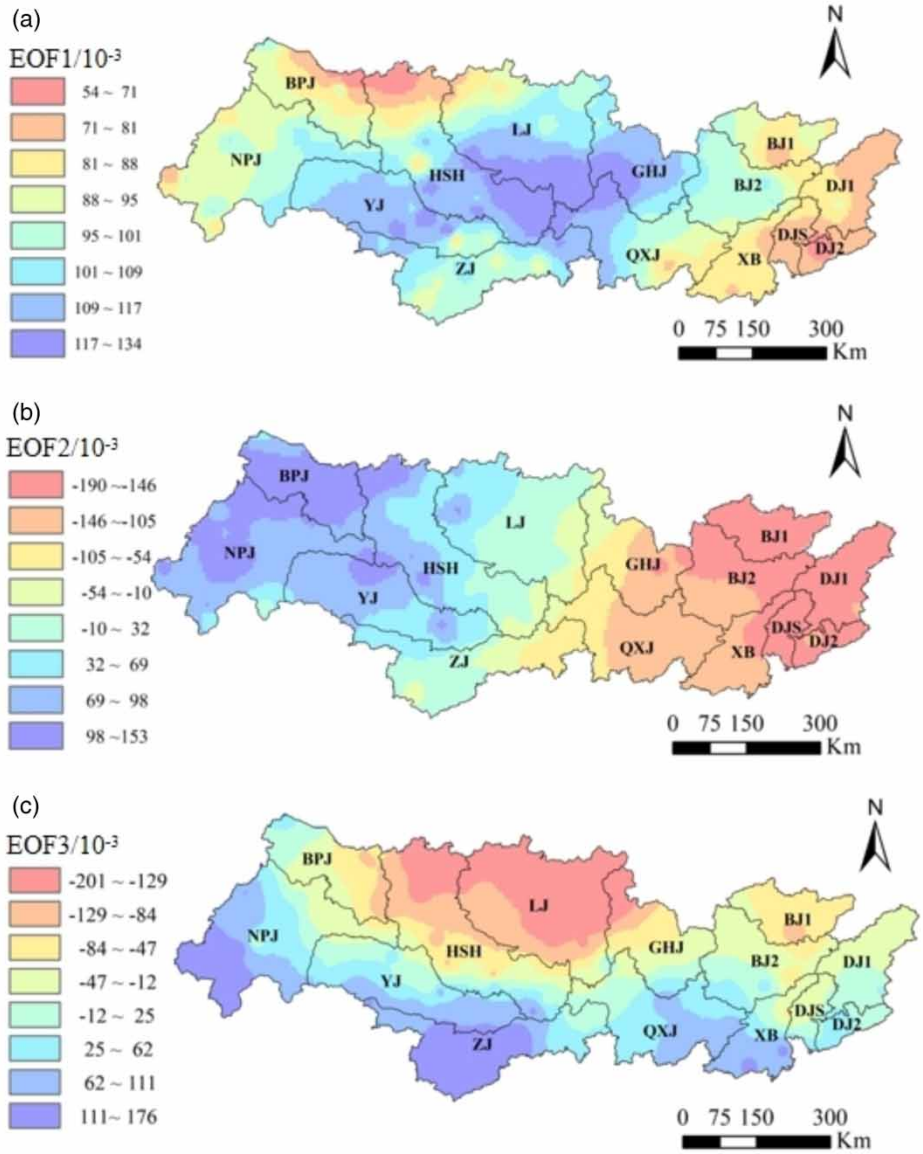

Figure 3 | The spatial distribution of the first three modes of the SPEI-12 decomposed by EOF: (a) EOF1, (b) EOF2 and (c) EOF3 represent mode 1, mode 2 and mode 3, respectively.

the central-south-type drought corresponding to mode 3, the central-north-type drought corresponding to mode 4 and the eastern-type drought corresponding to mode 5. Each drought type is divided according to the geographical location of the PRB, indicating that drought occurs in this region.

3.2. Temporal evolution characteristics of the drought field

Each time coefficient (RPC1–RPC5) corresponding to the first five modes obtained by REOF decomposition in the PRB was decomposed by ESMD to acquire three IMF components as well as a trend item R, as shown in Figure 5. It was discovered that each original time coefficient series coincided with the sum of the IMF components and the trend item R, indicating that the decomposition result was reliable.

3.2.1. Periodic characteristics

By FFT of IMF components, we could obtain the periodic characteristics of the time coefficient series decomposed by REOF (Table 3). Since IMF components as well as trend item R were independent from each other, the variance contributions were

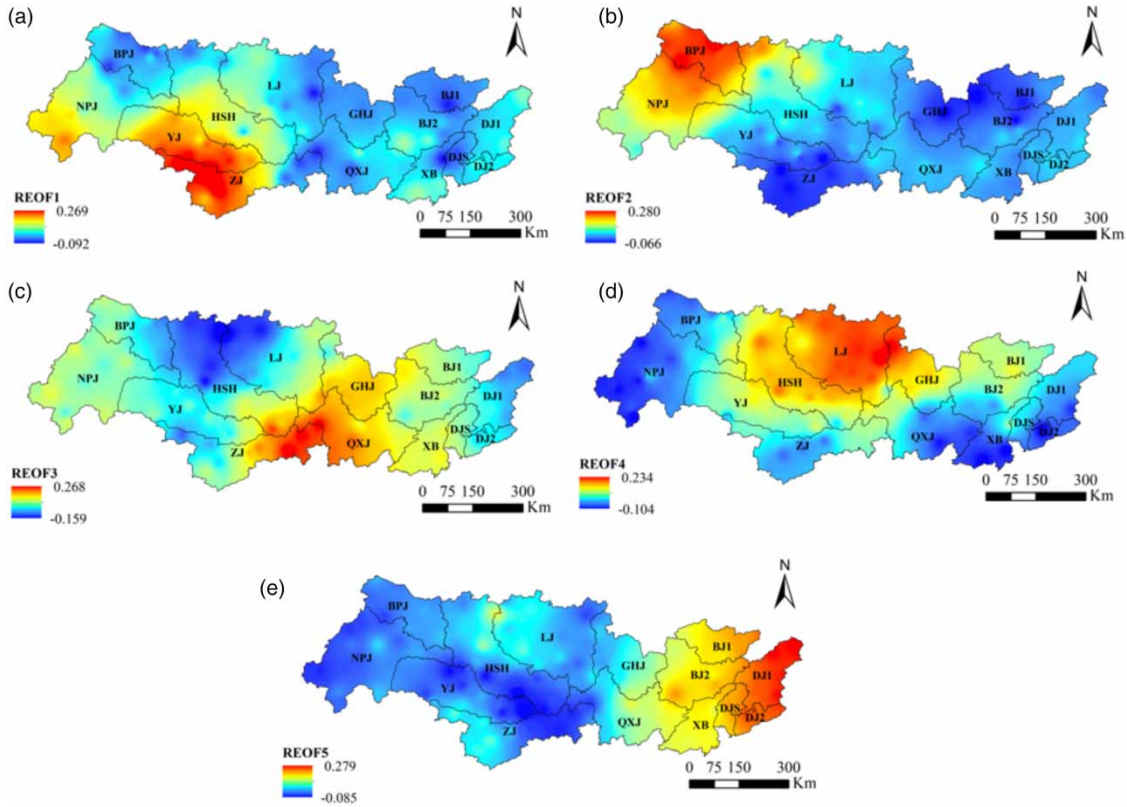

Figure 4 | The spatial distribution of the first five modes of SPEI-12 decomposed by REOF: (a) REOF1, (b) REOF2, (c) REOF3, (d) REOF4 and (e) REOF5 represent mode 1, mode 2, mode 3, mode 4 and mode 5, respectively.

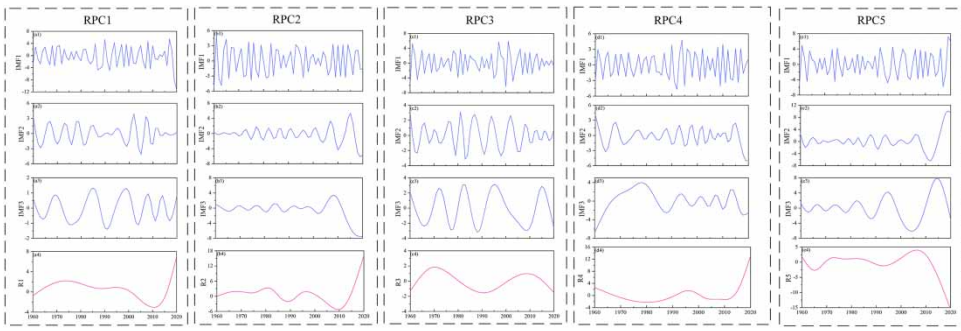

Figure 5 | The IMF components and trend item *R* of the time coefficients (RPC1–RPC5) of different drought types in the PRB after ESMD.

used to reflect the contribution of IMF components and trend item *R* to the volatility change of the original time coefficient series. The correlation between IMF components, trend item *R* and the initial time coefficient series was depicted using the Pearson correlation coefficient.

RPC1 had periodic characteristics of 2.21 years, 5.64 years and 12.4 years. Among the three IMF components, the variance contribution rate of IMF1 was the largest, reaching 62.17%, and the correlation coefficient was also the largest, reaching 0.716, which passed the significance test of $\alpha = 0.01$, indicating that 2.21 years was the main interannual variation cycle of southwest-type drought in the PRB. The variance contribution rate of IMF2 reached 15.68%, and the correlation coefficient was 0.352, which also passed the significance test of $\alpha = 0.01$, indicating that 5.64 years was the secondary interannual variation cycle of southwest-type drought in the PRB. The correlation coefficient of IMF3 failed to satisfy the significance level test of $\alpha = 0.01$ and 0.05, indicating that the 20.67-year cycle was not significant in the southwest-type drought of the PRB.

Table 3 | Periodic characteristics of the time coefficients decomposed by REOF

Mode	Time coefficient		Cycle/a	Variance contribution	Correlation coefficient
1	RPC1	IMF1	2.21	62.17%	0.716**
		IMF2	5.64	15.68%	0.352**
		IMF3	12.4	3.34%	0.143
		R	–	18.81%	0.298*
2	RPC2	IMF1	2.95	24.17%	0.682**
		IMF2	7.75	13.02%	0.298*
		IMF3	20.67	18.17%	0.009
		R	–	44.64%	0.302*
3	RPC3	IMF1	2.21	50.38%	0.718**
		IMF2	6.89	16.32%	0.294*
		IMF3	10.33	26.21%	0.438**
		R	–	7.09%	0.185
4	RPC4	IMF1	2.95	27.76%	0.733**
		IMF2	7.75	13.61%	0.159
		IMF3	31	23.01%	0.275*
		R	–	35.63%	0.281*
5	RPC5	IMF1	3.65	23.21%	0.704**
		IMF2	15.5	20.30%	0.118
		IMF3	20.67	23.63%	0.306*
		R	–	32.86%	0.110

Note: * and ** indicate passing the significance test of $\alpha = 0.05$ and $\alpha = 0.01$, respectively.

RPC2 had periodic characteristics of 2.95 years, 7.75 years and 20.67 years. Among the three IMF components, the correlation coefficients of IMF1 and IMF2 passed the significance tests of $\alpha = 0.01$ and 0.05, respectively, and the variance contribution rate of IMF1 was greater than that of IMF2, indicating that 2.95 years was the main interannual variation cycle of northwest-type drought in the PRB, and 7.75 years was the secondary interannual variation cycle of northwest-type drought in the PRB. The significance level test for the correlation coefficient for IMF3 failed at $\alpha = 0.01$ and 0.05, indicating that the 20.67-year cycle was not significant in the southwest-type drought of the PRB.

RPC3 had periodic characteristics of 2.21 years, 6.89 years and 10.33 years. Among the three IMF components, the variance contribution rate of IMF1 was the largest, reaching 50.38%, and the correlation coefficient was also the largest, reaching 0.718, which passed the significance test of $\alpha = 0.01$, indicating that 2.21 years was the main interannual variation cycle of south-central-type drought in the PRB. The variance contribution rate of IMF2 reached 16.32%, and the correlation coefficient was 0.294, which passed the significance test of $\alpha = 0.05$, indicating that 6.89 years was the secondary interannual variation cycle of south-central-type drought in the PRB. The correlation coefficient of IMF3 passed the significance test of $\alpha = 0.01$, and the variance contribution rate was 26.21%, indicating that 10.33 years was the interdecadal variation cycle of south-central-type drought in the PRB.

RPC4 had periodic characteristics of 2.95 years, 7.75 years and 31 years. Among the three IMF components, the variance contribution rate of IMF1 was 27.76%, and the correlation coefficient was the largest, reaching 0.733, which passed the significance test of $\alpha = 0.01$, indicating that 2.95 years was the interannual variation cycle of north-central-type drought in the PRB. The variance contribution rate of IMF2 was the smallest, and the correlation coefficient was also the smallest, which failed to satisfy the significance test of $\alpha = 0.01$ and 0.05, indicating that the 7.75-year cycle was not significant in the north-central-type drought in the PRB. The variance contribution rate of IMF3 was 23.01%, and the correlation coefficient was 0.275, which passed the significance test of $\alpha = 0.05$, indicating that 31 years was the interdecadal variation cycle of north-central-type drought in the PRB.

RPC5 had periodic characteristics of 3.65 years, 15.5 years and 20.67 years. Among the three IMF components, the variance contribution rate of IMF1 was 23.21%, and the correlation coefficient was the largest, reaching 0.704, which passed the significance test of $\alpha = 0.01$, indicating that 3.65 years was the interannual variation cycle of eastern-type drought in the PRB. The variance contribution rate of IMF2 was the smallest, and the correlation coefficient was also the smallest, which failed to satisfy the significance test of $\alpha = 0.01$ and 0.05, indicating that the 15.5-year cycle was not significant in

the eastern-type drought of the PRB. The variance contribution rate of IMF3 was 23.63%, and the correlation coefficient was 0.306, which passed the significance test of $\alpha = 0.05$, indicating that 31 years was the interdecadal cycle of the eastern-type drought.

3.2.2. Trend features

After the time coefficients of the five modes were decomposed by ESMD, we obtained the trend item *R*, as shown in Figure 5.

The trend item *R* of RPC1 was roughly divided into the early 21st century, showing different characteristics of change. The fluctuation was relatively slow before the 21st century, and greatly shifted after the 21st century. During the study period, 1974 was at the positive peak, and 2011 was at the trough. The curve showed an upward trend after 2011 and exceeded the positive peak in 2018, indicating that the southwest-type drought in the PRB was relatively typical in 1974 and after 2018, while the southwest-type drought in the PRB in 2011 was not typical.

The trend item *R* of RPC2 was at the positive peak in 1981 and 1998. The curve was in the rising stage from 2009 to 2020 and exceeded the previous positive peak in 2016, indicating that the northwest-type drought in the PRB was typical in these periods. However, it was in the valley value period in 2010, indicating that the northwest-type drought in the PRB in 2010 was not typical.

The trend item *R* of RPC3 was at the positive peak in 1970 and 2009, indicating that the south-central-type drought in the PRB was relatively typical in these periods, while it was in the valley period in 1991, indicating that the south-central-type drought in the PRB was not typical in 1991.

The trend item *R* of RPC4 experienced two 'decrease–increase' changes in the study period and was in the valley period in 1980 and 2010, indicating that the north-central-type drought in the PRB was not typical during this time range. After 2010, the curve had an increasing trend, indicating that the PRB's north-central-type drought had seen a comeback.

The trend item *R* of RPC5 reached a valley period in 1965, after which the curve fluctuated more smoothly. The curve reached a positive peak in 2006, then showed a downward trend, and was lower than the valley value in 2015, indicating that the eastern-type drought in the PRB in 1965 and 2015 was not significant, while the eastern-type drought in the PRB in 2006 was relatively typical.

In general, the trend item *R* of RPC1, RPC2 and RPC4 presented an upward trend approximately 2010, implying that the southwest-type drought, northwest-type drought and north-central-type drought in the PRB had a recovery trend after 2010. However, the trend item *R* of RPC3 presented a declining trend approximately 2010, implying that the south-central-type drought in the PRB had a trend of mitigation after 2010. The trend item *R* of RPC5 presented a declining trend approximately 2006, implying that the eastern drought in the PRB had this mitigation trend after 2006.

3.2.3. Comparison of interannual and interdecadal variations in different spatial distribution types of drought field

To identify the interannual as well as interdecadal similarities and differences in the five spatial distribution types of drought field in the PRB, the IMF components of the time coefficients (RPC) were classified into IMF components with an interannual cycle (IMF-interannual) and IMF components with an interdecadal cycle (IMF-interdecadal). IMF-interannual is a small-scale oscillation curve, while IMF-interdecadal is a large-scale oscillation curve. Summing all IMF components with interannual periods and adding them to the trend item *R*, we obtain the interannual variation curve of time coefficients (containing small-scale oscillation and filtering out large-scale oscillation), and similarly summing all IMF components with interdecadal periods and adding them to the trend item *R*, we obtain the interdecadal variation curve of time coefficients (retaining large-scale oscillation and filtering out small-scale oscillation). The interannual and interdecadal variation curves of time coefficients represent the interannual and interdecadal trends of the drought field in the PRB, respectively, as shown in Figure 6.

From the perspective of interannual variation, the time coefficients of each mode have both similarities and differences. The variation trends of RPC1 and RPC2 before 2000 were similar, and the fluctuation range was small, indicating that the interannual variations in the southwest-type drought and northwest-type drought showed similar characteristics. RPC1 grew and then declined after the year 2000, whereas RPC2 decreased and then increased, indicating that the interannual variation in the southwest-type drought and northwest-type drought showed the opposite characteristics. The fluctuation ranges of RPC4 and RPC5 were relatively consistent before 2010. After 2010, RPC4 showed an overall upward trend, while RPC5 showed an overall downward trend, indicating that the interannual variations in the central-north-type drought and eastern-type drought showed similar characteristics before 2010, while they were opposite after 2010.

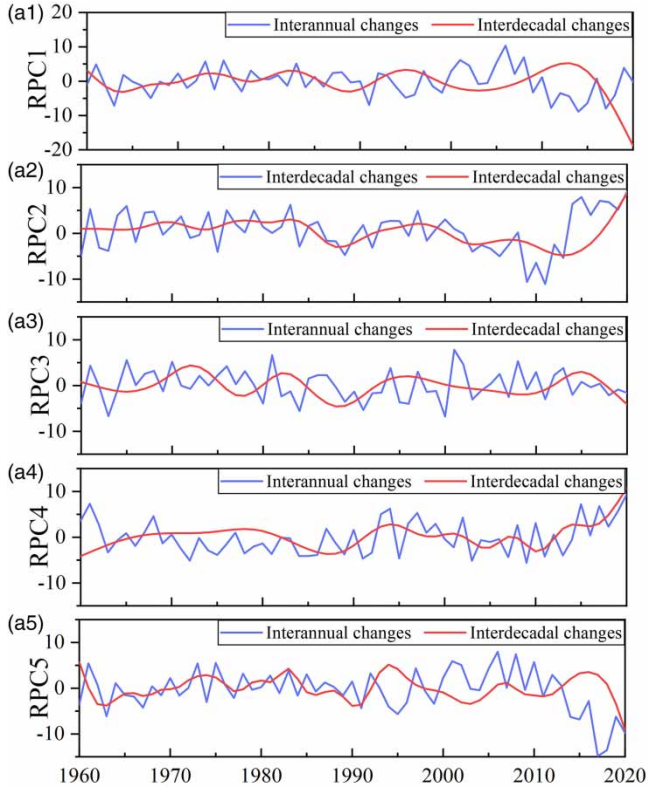

Figure 6 | Interannual and interdecadal variation of time coefficients (RPC1–RPC5) of different drought types in the PRB.

The interdecadal variations of RPC1, RPC3 and RPC5 were relatively consistent except for the individual years, which indicated that the interdecadal variations of the southwest-type drought, the central-south-type drought and the eastern-type drought in the PRB showed similar characteristics.

4. CONCLUSION AND DISCUSSION

- The EOF decomposition showed that the interannual drought in the PRB had three main distribution patterns: the whole basin consistent type, the east–west antiphase type and the west, south–north antiphase type. The whole basin consistent was the main type.
- According to the REOF decomposition, there are five distinct types of interannual drought that can be identified in the PRB: southwest-type drought, northwest-type drought, south-central-type drought, north-central-type drought, and eastern-type drought. The five types were the main spatial distribution of interannual drought in the PRB. REOF decomposition is better than EOF decomposition in revealing the local characteristics of drought in the watershed.
- The southwest and northwest-type droughts had interannual variation periods. The south-central, north-central, and eastern-type droughts had both interannual and interdecadal variation periods.
- During the study period, the PRB's five types of droughts revealed a changing tendency as opposed to a straightforward linear trend. After 2010, the southwest, northwest and north-central-type droughts presented a rising trend, while the south-central-type drought showed a moderating trend, and the eastern-type drought showed a moderating trend after 2006.
- The five drought types had both similarities and differences in the interannual and interdecadal timescales. From the interannual variation, the southwest-type drought was consistent with the northwest-type drought prior to 2000, but they became distinct after 2000. Before 2010, the north-central-type drought and the eastern-type drought were consistent; however, after 2010, they also became distinct. From the interdecadal variation, the southwest-type drought, central-south-type drought and eastern-type drought shared the most similarities, while the northwest-type drought and the central-north-type drought were most similar.

With the intensification of global warming, the problem of drought in China has become increasingly prominent. The high frequency, long duration and wide impact of drought disasters can have a significant impact on regional socioeconomics and environment (Yang *et al.* 2015). The drought-prone areas show an expansion to the wet and semihumid areas in the south and east (Zhang & Zhou 2015). In recent years, with the intensification of climate change and the impact of human activities, drought in the PRB has become a serious problem. In the study of drought field, Jing *et al.* (2021) identified drought field in the PRB from 1960 to 2019 based on the SPI and EOF analysis, and a total of three drought types were identified, which are consistent with the first three drought types of drought field identified in this paper. The literature on the REOF method to study the drought field in the PRB is relatively small, mostly focusing on the pre-2011 period. Chen (2020) divided the drought field of the PRB into eastern-type drought, north-central-type drought, south-central-type drought, southwestern-type drought, northwestern-type drought and western-type drought. The eastern-type drought was the most typical, while the northwest-type drought and western-type drought were not typical. The reason for this difference may be that the research timescale was from 1961 to 2011. In recent years, the drought in the eastern part of the PRB had a trend of mitigation, while the drought in the western part had a trend of aggravation (Xiao *et al.* 2012; Jing *et al.* 2021). The five kinds of drought in the PRB all had the periodic characteristics of 2–7 years, which may be affected by 'El Nino' and 'La Nina' (Tang & Yuan 2010; Chen 2020). Some drought types had the periodic characteristics of 10.33 and 20.67 years, which may be related to sunspot activity. After 2006, the eastern-type drought of the PRB had a trend of mitigation, which was basically agreed with the result of Jing *et al.* (2021). During the period from 2020 to 2021, two La Niña events occurred (Qian & Lu 2022), resulting in poor water vapor conditions in the southern region, which led to precipitation in the eastern PRB to significantly decline. Therefore, the eastern-type drought of the PRB has been rebounding since 2020.

Based on SPEI-12 of 61a, the drought field in the PRB was detected. Five different kinds of droughts' periodic characteristics and trend features were examined, which could provide a scientific basis for drought monitoring in the watershed. The PRB is a large area, and the interannual and interdecadal variability of each subregion is influenced by its geographical location, land surface topographic structure and hydroclimate, which have both similarities and differences, but the influence mechanisms are not fully understood, which is the focus of future research.

ACKNOWLEDGEMENTS

The National Key Research and Development Program of China (2021YFC3200204) and the National Natural Science Foundation of China (52079125) provided funding for this work.

DATA AVAILABILITY STATEMENT

Data cannot be made publicly available; readers should contact the corresponding author for details.

CONFLICT OF INTEREST

The authors declare there is no conflict.

REFERENCES

Band, S. S., Karami, H., Jeong, Y. W., Moslemzadeh, M., Farzin, S., Chau, K. W., Bateni, S. M. & Mosavi, A. 2022 Evaluation of time series models in simulating different monthly scales of drought index for improving their forecast accuracy. *Frontiers in Earth Science* **10**, 839527. https://doi.org/10.3389/feart.2022.839527.

Barriopedro, D., Gouveia, C. M., Trigo, R. M. & Wang, L. 2012 The 2009/10 drought in China: possible causes and impacts on vegetation. *Journal of Hydrometeorology* **13** (4), 1251–1267. https://doi.org/10.1175/JHM-D-11-074.1.

Bi, S. B., Qiu, X. K., Wang, G. J., Gong, Y. C., Wang, L. Y. & Xu, M. Y. 2021 Spatial distribution characteristics of drought disasters in Hunan Province of China from 1644 to 1911 based on EOF and REOF methods. *Environmental Earth Sciences* **80** (16), 1–11. https://doi.org/10.1007/s12665 -021-09867-1.

Chen, Z. S. 2020 Empirical diagnostic analysis on spatial and temporal variations of droughts in the Pearl River basin. *Acta Scientiarum Naturalium Universitatis Sunyatseni* **59** (4), 33–42. https://doi.org/10.13471/j.cnki.acta.snus.2019.09.22.2019D038.

Chen, H. P. & Sun, J. Q. 2015 Changes in drought characteristics over China using the standardized precipitation evapotranspiration index. *Journal of Climate* **28** (13), 5430–5447. https://doi.org/10.1175/JCLI-D-14-00707.1.

Deng, Z. F., Wu, X. S., Wang, Z. L., Li, J. & Chen, X. H. 2020 Drought monitoring based on GRACE data in the Pearl River Basin. *Transactions of the Chinese Society of Agricultural Engineering* **36** (20), 179–187. https://doi.org/10.11975/j.issn.1002-6819.2020.20.021.

Duhamel, P. & Vetterli, M. 1990 Fast Fourier transforms: a tutorial review and a state of the art. *Signal Processing* **19** (4), 259–299. https://doi.org/10.1016/0165-1684(90) 90158-U.

Feng, K. & Su, X. L. 2019 Spatiotemporal characteristics of drought in the Heihe River Basin based on the extreme-point symmetric mode decomposition method. *International Journal of Disaster Risk Science* **10**, 591–603. https://doi.org/10.1007 /s13753-019-00241-1.

Gbetibouo, G. A. & Hassan, R. M. 2005 Measuring the economic impact of climate change on major South African field crops: a Ricardian approach. *Global and Planetary Change* **47** (2–4), 143–152. https://doi.org/10.1016/j.gloplacha.2004.10.009.

Hang, Y. C., Fan, M. T. & Liu, Z. Y. 2022 Spatiotemporal variation of water level in Pearl River Delta network area based on REOF. *Water Resources Protection* **38** (2), 139–146. https://doi.org/10.3880/j.issn.1004-6933.2022.02.019.

Heudorfer, B. & Stahl, K. 2017 Comparison of different threshold level methods for drought propagation analysis in Germany. *Hydrology Research* **48**, 1311–1326. https://doi.org/10.2166/nh.2016.258.

Huang, Q., Chen, Z. S., Liu, Z. M. & Kong, L. 2013 Regional drought risk assessment across the Pearl River basin. *Acta Scientiarum Naturalium Universitatis SunYatseni* **52** (5), 141–152. https://doi.org/10.13471/j.cnki.acta.snus.2013.05.026.

Huang, Q., Chen, Z. S., Tang, C. Y. & Li, S. F. 2019 Monitoring the spatio-temporal process of severe droughts in the Pearl River Basin. *Advances in Earth Science* **34** (10), 1050–1059. https://doi.org/10.11867/j.issn.1001-8166.2019.10.1050.

Jeong, J. S., Kim, Y. S., Baek, K. H., Jung, H., Ha, S. H., Choi, Y. D., Kim, M., Reuzeau, C. & Kim, J. 2010 Root-specific expression of OsNAC10 improves drought tolerance and grain yield in rice under field drought conditions. *Plant Physiology* **153** (1), 185–197. https://doi.org/10.1104/pp.110.154773.

Jiang, P., Liu, H. Y., Wu, X. C. & Wang, H. Y. 2017 Tree-ring-based SPEI reconstruction in central Tianshan Mountains of China since AD 1820 and links to westerly circulation. *International Journal of Climatology* **37** (6), 2863–2872. https://doi.org/10.1002/joc.4884.

Jing, J. L., Xu, Y., Wang, Y. F., Dou, S. Q. & Yin, M. 2021 Characteristics of multi-scale drought and flood in the Pearl River Basin from 1960 to 2019. *Research of Agricultural Modernization* **42** (03), 557–569. https://doi.org/10.13872/j.1000-0275.2021.0065.

Kim, K. Y., Hamlington, B. & Na, H. 2015 Theoretical foundation of cyclostationary EOF analysis for geophysical and climatic variables: concepts and examples. *Earth-science Reviews* **2015** (150), 201–218. https://doi.org/10.1016/j.earscirev.2015.06.003.

Li, J., Peng, R. & Li, D. Q. 2019 Effects of ion size, ion valence and pH of electrolyte solutions on EOF velocity in single nanochannels. *Analytica Chimica Acta* **1059**, 68–79. https://doi.org/10.1016/j.aca.2019.02.008.

Ling, M. H., Guo, X. M., Shi, X. L. & Han, H. B. 2022 Temporal and spatial evolution of drought in Haihe River Basin from 1960 to 2020. *Ecological Indicators* **138**, 108809. https://doi.org/10.1016/j.ecolind.2022.108809.

Luo, L. X., Jiang, T., Sun, H. M., Jing, C. & Su, B. D. 2017 Variation of droughts and floods and their connection with atmospheric circulation in the Pearl River basin. *Journal of Arid Land Resources and Environment* **31** (4), 142–147. https://doi.org/10.13448/j.cnki.jalre.2017.124.

North, G. R., Bell, T. L., Cahalan, R. F. & Moeng, F. J. 1982 Sampling errors in the estimation of empirical orthogonal functions. *Monthly Weather Review* **110** (7), 699–706. https://doi.org/10.1175/1520-0493(1982)110<0699:SEITEO > 2.0.CO;2.

Qi, L. Q., Su, X. L. & Feng, K. 2020 Response of multi-scale meteorological drought to circulation index in northwest China. *Journal of Arid Land Resources and Environment* **34** (1), 106–114. https://doi.org/10.13448/j.cnki.jalre.2020.015.

Qian, Y. & Lu, K. M. 2022 Brief analysis and thoughts on the drought of the Pearl River basin in 2021. *China Flood & Drought Management* **32** (6), 27–30. https://doi.org/10.16867/j.issn.1673-9264.2022163.

Sahana, V., Mondal, A. & Sreekumar, P. 2021 Drought vulnerability and risk assessment in India: sensitivity analysis and comparison of aggregation techniques. *Journal of Environmental Management* **299**, 113689. https://doi.org/10.1016/ j.jenvman.2021.113689.

Saharwardi, M. S. & Kumar, P. 2022 Future drought changes and associated uncertainty over the homogenous regions of India: a multimodel approach. *International Journal of Climatology* **42** (1), 652–670. https://doi.org/10.1002/ joc.7265.

Shi, L., Feng, P., Wang, B., Liu, D. & Yu, Q. 2020 Quantifying future drought change and associated uncertainty in southeastern Australia with multiple potential evapotranspiration models. *Journal of Hydrology* **590**, 125394. https://doi.org/10.1016/j.jhydrol.2020.125394.

Song, C. & Chen, X. H. 2021 Performance comparison of machine learning models for annual precipitation prediction using different decomposition methods. *Remote Sensing* **13** (5), 1018. https://doi.org/10.3390/rs13051018.

Song, X. Y., Lu, F., Wang, H., Xiao, W. H. & Zhu, K. 2018 Penalized maximum likelihood estimators for the nonstationary Pearson type 3 distribution. *Journal of Hydrology* **567**, 579–589. https://doi.org/10.1016/ j.jhydrol.2018.10.035.

Sun, Y. 2021 Impact of humanactivities on climate system: an interpretation of Chapter III of WGIreport of IPCC AR6. *Transactions of Atmospheric Sciences* **44** (05), 654–657. https://doi.org/10.13878/j.cnki. dqkxxb.20210816009.

Sun, P., Ma, Z., Zhang, Q., Singh, V. P. & Xu, C. Y. 2022 Modified drought severity index: model improvement and its application in drought monitoring in China. *Journal of Hydrology* **612**, 128097. https://doi.org/10.1016/j.jhydrol.2022.128097.

Tang, X. C. & Yuan, Z. Y. 2010 The influence of the drought disaster caused by El Nino events in Guangdong Province in recent 60 years. *Geographical Research* **29** (11), 1932–1939.

Ureta, C., González, E. J., Espinosa, A., Trueba, A., Piñeyro-Nelson, A. & Álvarez-Buylla, E. R. 2020 Maize yield in Mexico under climate change. *Agricultural Systems* **177**, 102697. https://doi.org/10.1016/j.agsy.2019.102697.

Van Loon, A. F., Gleeson, T., Clark, J., Van Dijk, A. I. J. M., Stahl, K., Hannaford, J., Di Baldassarre, G., Teuling, A. J., Tallaksen, L. M., Uijlenhoet, R., Hannah, D. M., Sheffield, J., Svoboda, M., Verbeiren, B., Wagener, T., Rangecroft, S., Wanders, N. & Van Lanen, H. A. J. 2016 Drought in the anthropocene. *Nature Geoscience* **9**, 89–91. https://doi.org/10.1038/ngeo2646.

Wang, J. L. & Li, Z. J. 2013 Extreme-point symmetric mode decomposition method for data analysis. *Advances in Adaptive Data Analysis* **5**, 1350015. https://doi.org/10.1142/S17935369 13500155.

Wang, F., Lai, H. X., Li, Y. B., Feng, K., Zhang, Z. Z., Tian, Q. Q., Zhu, X. M. & Yang, H. B. 2022 Dynamic variation of meteorological drought and its relationships with agricultural drought across China. *Agricultural Water Management* **261**, 107301. https://doi.org/10.1016/j.agwat.2021.107301.

Won, J., Choi, J., Lee, O. & Kim, S. 2020 Copula-based Joint Drought Index using SPI and EDDI and its application to climate change. *Science of the Total Environment* **744**, 140701. https://doi.org/10.1016/j.scitotenv.2020.140701.

Xiao, M. Z., Zhang, Q. & Chen, X. H. 2012 Spatial-temporal patterns of drought risk across the Pearl River Basin. *Acta Geographica Sinica* **67** (1), 83–92.

Xie, L. W., Luo, L. F., Ma, J. J., Li, Y., Zhang, M. M., Zeng, X. J. & Cao, Y. J. 2022 A novel fault location method for hybrid lines based on traveling wave. *International Journal of Electrical Power & Energy Systems* **141**, 108102. https://doi.org/10.1016/j.ijepes.2022.108102.

Yang, J. H., Zhang, Q., Wang, J. S., Yao, Y. B. & Shang, J. L. 2015 Extreme and persistent feature of drought and flood of southwest China in past 60 years. *Scientia Geographica Sinica* **35** (10), 1333–1340. https://doi.org/10.13249/j.cnki.sgs.2015.10.017.

Zhan, C., Liang, C., Zhao, L., Jiang, S. Z., Niu, K. J. & Zhang, Y. L. 2022 Drought-related cumulative and time-lag effects on vegetation dynamics across the Yellow River Basin, China. *Ecological Indicators* **143**, 109409. https://doi.org/10.1016/ j.ecolind.2022.109409.

Zhang, L. X. & Zhou, T. J. 2015 Drought over East Asia: a review. *Journal of Climate* **28** (8), 3375–3399. https://doi.org/10.1175/JCLI-D-14-00259.1.

Zhang, H. W., Song, J., Wang, G., Wu, X. Y. & Li, J. 2021 Spatiotemporal characteristic and forecast of drought in northern Xinjiang, China. *Ecological Indicators* **127**, 107712. https://doi.org/10.1016/j.ecolind.2021.107712.

Zhao, F., Bi, S. B., Li, X. Y., Wu, W. T. & Jiang, T. T. 2019 Spatial characteristics of drought/flood disasters based on EOF and REOF in the middle and lower reaches of the Yellow River from 1470 to 1911. *Arid Land Geography* **42** (4), 799–809. doi: 10.12118/j.issn.1000-.6060.2019.04.11.

Zhou, J. G., Huo, X. J., Xu, X. L. & Li, Y. S. 2019 Forecasting the carbon price using extreme-point symmetric mode decomposition and extreme learning machine optimized by the grey wolf optimizer algorithm. *Energies* **12** (5), 950. https://doi.org/10.3390/en12050950.

Zhou, Z., Shi, H., Fu, Q., Li, T., Gan, T. Y. & Liu, S. 2020 Assessing spatiotemporal characteristics of drought and its effects on climate-induced yield of maize in Northeast China. *Journal of Hydrology* **588**, 125097. https://doi.org/10.1016/ j.jhydrol.2020.125097.

Zuo, D. P., Cai, S. Y., Xu, Z. X., Peng, D. Z., Kan, G. Y., Sun, W. C., Pang, B. & Yang, H. 2019 Assessment of meteorological and agricultural droughts using in-situ observations and remote sensing data. *Agricultural Water Management* **222**, 125–138. https://doi.org/10.1016/j.agwat.2019.05.046.

First received 15 March 2023; accepted in revised form 9 June 2023. Available online 22 June 2023